Article

Ultrasound induced Stroboscopic Optical Elastography (SOE) of cells

Thomas Combriat[1,2,3], Petter Angell Olsen[2,4], Anders Malthe-Sørenssen[1,3], Stefan Krauss[2,4], and Dag Kristian Dysthe[1,*]

[1]University of Oslo, Department of Physics, Njord Centre, P.O. Box 1048 Blindern, 0316 Oslo, Norway
[2]University of Oslo, Hybrid Technology Hub, Institute of Basic Medical Sciences P.O. Box 1110 Blindern, 0317 OSLO, Norway
[3]University of Oslo, Center for Computing in Science Education, P.O. Box 1048 Blindern, 0316 Oslo, Norway
[4]Oslo University Hospital, Department of Immunology and Transfusion Medicine, P.O. Box 4950, Nydalen, 0424 Oslo, Norway
[*]Correspondence: dagkd@fys.uio.no

ABSTRACT   Lorem ipsum

SIGNIFICANCE   aunisretaunirest

---

1 INTRODUCTION

1.1 TODO

- STL file in suppM

- https://pubmed.ncbi.nlm.nih.gov/29661978/

- mention both strains only once, plot the average in the following, put the two in SM.

- make a Supplementary Material video

- Diagnostics

  - Shear-wave and strain elastography: commonly used in US diagnostic to probe the shear modulus of material by measuring its response to a mechanical stimuli, used in identification of liver fibrosis (1, 2), identification of malignous tumours (3–6). Only works in vivo, poor resolution, big scanned area. Frequency > MHz (7, 8). Low frequency, high resolution, small areas.

- Basic science and mechanotransduction

  - Complete opposite of the spectrum: AFM is super high resolution, and is used in biological context for basic science purposes (9) in applications as wide

  - Microfluidics (10): usage of microfluidics to stimulate cells at fairly high frequencies

  - quantitative deformability cytometry (11)

  - traction force microscopy: mechanical input of biological material on a substrate but no stimuli (12)

  - optical elastography (that's us) (13).

  - Cell mechanotyping EMT mechanotyping using AFM (attached cells), and deformability cytometry (suspended cells) (14) (Amy Rowat group). High throughput deformability assay (suspended cells) (15).

- Holographic Cell Stiffness Mapping Using Acoustic Stimulation (16)

- Shear wave elastography in vitro (17).

- particle tracking microrheology (18)

- optical and acoustic trapping???

1.2 Measurement of cell stiffness

1.2.1 Attempt1

Being able to measure the stiffness of cells or tissues is of great interest in clinical diagnostics where US-based shear-wave and strain elastography (19) and magnetic resonance elastography (13) are commonly used for example to identify fibrosis (1, 2) or tumors (3–6). These techniques take advantage of the deep penetration of both US and electromagnetic waves to provide non-invasive, three dimensional stiffness information of tissues deep inside the body at the scale of the organs or part of organs which are useful to physicians. However, because of the apparatus needed and their limited resolution, these techniques are not very useful for *in vitro* studies on mechanobiology which are dealing with single cells, cell colony and organoids.

Optical elastography techniques, like optical coherence elastography (OCE) (20, 21) and Brillouin microscopy (22), alleviate the low resolution of clinical measurements by using optics, trading off penetration depth of the measurements for resolution while keeping three dimensional capacity. OCE works by recovering the strains in the studied material in response to a load using low-coherence interferometry. Different types of loads can be used, ranging from quasi-static ($f < 10 − 50$ Hz) uniform loading (23), harmonic where an periodic load is applied continuously by the mean of acoustic waves or air puff and standing waves forming in the material are imaged to recover its mechanical properties at the loading frequency ($50 − 500$ Hz) and transient where impulse loading is applied and mechanical properties are estimated from the propagation of the acoustic wave in the media of interest. OCE, alongside Brillouin microscopy which is using the scattering of light by phonons propagating in the studied in the material, have three dimensional capability and have been used for both in vitro, for instance to study cell mechanics (24), and in vivo (ophtalmology).

Probably brillouin should be separated. OCE, which is the closest to what we do, might need to be put last.

[Transition big problem since I added OCE...] Pure in vitro studies on the other hand are not impede by this penetration problem, their subject sizes ranging from the single cell to organoids. For this reason, different techniques exists for recovering mechanical information of biological material in vitro. These techniques differ principally with the spatial resolution they can achieve, their throughput, the frequency range at which they operate, the type of data they produce and the ease of implementation. On these matters, Atomic Force Microscopy (AFM) for example is a contrasting example with the techniques used in clinics. In AFM, the deflection of a cantilever of known rigidity is measured very precisely. This can be used to indent biological material with a known stress/force and, from the resulting indentation, the stiffness of the probed material. This technique has been successfully used to perform single cell elastography (9, 14, 25). AFM being a point measure, scanning through the whole sample is necessary to acquire elastographic maps. The very high resolution, allowing for sub-cellular features to be studied, and quality of the results are unfortunately impeded by a low throughput and a limitation on the attainable frequencies ($1 − 1000$ Hz).

The greater or lesser ability for cells to squeeze, which is directly linked to their stiffness, has also been used to perform high-throughput mechanotyping. Using deformability cytometry (14), or constriction based devices (15, 26). These approaches have shown the ability to differentiate and to separate metastatic cancer cells to normal ones. In contrast to AFM, these techniques do not recover any mechanical information about sub-cellular components: deformability of whole cells as assessed as a whole allowing for fast diagnostics of potentially malignant cells which are useful to physicians.

1.2.2 Attempt2

- Add microrheology with optical tweezers/acoustics tweezer,

- add microrheology (with PTV)

- Add more about limitations (type of cells studied)

A lot of different techniques exist to recover mechanical information, like stiffness, of biological material for both in vivo and in vitro studies. Depending on the sought information these techniques have different balance between the probed frequency, the resolution, the capacity to recover or not three-dimensional information and the throughput. Being able to measure the stiffness of cells or tissues is of great interest in clinical diagnostics where US-based shear-wave and strain elastography (19) and magnetic resonance elastography (13) are commonly used for example to identify fibrosis (1, 2) or tumors (3–6). These techniques take advantage of the deep penetration of both US and electromagnetic waves to provide non-invasive, three dimensional stiffness information of tissues deep inside the body at the scale of the organs or part of organs which are useful to physicians. However, this deep penetration comes at the cost of resolution, which does not excedd the centimetric scale in these techniques. Therefor, these techniques have limited applications in in vitro studies on mechanobiology and mechanotransduction which are focused on cells, colonies and organoids.

Optical elastography techniques, like optical coherence elastography (OCE) (20, 21) and Brillouin microscopy (22), alleviate the low resolution of clinical measurements by using optics, trading off penetration depth of the measurements for

resolution while keeping three dimensional capacity. OCE works by recovering the strains in the studied material in response to a load using low-coherence interferometry. Different types of loads can be used, ranging from quasi-static ($f < 10 - 50$ Hz) uniform loading (23), harmonic where an periodic load is applied continuously by the mean of acoustic waves or air puff and standing waves forming in the material are imaged to recover its mechanical properties at the loading frequency ($50 - 500$ Hz) and transient where impulse loading is applied and mechanical properties are estimated from the propagation of the acoustic wave in the media of interest. TOADD: usage in clinics (ophtalmology). Brillouin microscopy on the other hand, do not require an external loading, but uses the scattering of the light by acoustic waves (phonons) propagating in the probed material (Brillouin light scattering (27)). This technique has recently be shown to recover mechanical information at both the scale of the single cell (28), and living small organism (29). A fundamental limitation of Brillouin microscopy lies in the very high frequency at which the mechanical properties are probed (GHz), way above both the viscoelastic transition (≈ 100 Hz) (30) of typical biological materials and the typical range of frequencies they are subjected in their normal environment. Therefor, the recovered properties are different from the ones measured for eg. atomic force microscopy (AFM), making them hard to compared with known standards.

For pure in vitro studies, where adherent cells are mostly used, AFM is considered a gold standard. In AFM, the deflection of a cantilever of known rigidity is measured very precisely while it is indenting a precise part of the probed substrate, recover the stiffness of biological material with very good resolution and precision allowing to perform single cell elastography (9, 14, 25). AFM being a point measure at the surface, scanning through the whole sample is necessary to acquire elastographic maps, three dimensional information is not recovered. The very high resolution, allowing for sub-cellular features to be studied, and quality of the results are impeded by a low throughput and a limitation on the attainable frequencies ($1 - 1000$ Hz).

The greater or lesser ability for cells to squeeze, directly linked to their stiffness, has also been used to perform high-throughput mechanotyping. Using deformability cytometry (14), or constriction based devices (15, 26), these approaches have shown the ability to differentiate and to separate metastatic cancer cells to normal ones. In contrast to more resolved techniques like AFM or OCE, these techniques do not recover any mechanical information about sub-cellular components: deformability of whole cells is assessed and allow to recover population of a particular mechanotype.

1.3 Stiffness of cells

Cell stiffness, defined as the ability of cells to resist deformation in response to applied forces (Young's modulus), is an important mechanical property of cells that is linked to various cellular behaviors. is "cell stiffness" an appropriate term to use??

The stiffness of a cell is determined by the composition of the nucleus and cytoplasm. The nucleus is the stiffest part of the cells and nuclear stiffness is mainly determined by the conformation of the chromatin and the structure of the lamin nucleoskeleton (31–33) (PMID: 15090601, 29227210, 10720492). The main cytoplasmic component that governs stiffness of cells is the organization of the cytoskeleton (actin filaments, microtubules, and intermediate filaments), however other cytoplasmic components like polymers of glycosaminoglycans and polysaccharides together with membrane tubes of the endoplasmic reticulum (ER) can also influence on cellular stiffness (34) (PMID: 29092896). Furthermore, the arrangement of focal adhesions mediating cell adhesion to the extracellular matrix and cell junctions connecting neighboring cells can influence on the stiffness of cells due to their association with the cytoskeleton (35) (PMID: 32830356).

Given the dyamic behavior of cytoskeleton organization, the stiffness of a cell is not constant and varies under normal conditions. For example during cell division the cell stiffness changes so that cells in the S cell cycle phase are generally stiffer relative to non-dividing cells in the G1 phase (36) (PMID: 21481877). Another central cellular process where cell stiffness is changed during cell migration where mobile cells generally display a softer phenotype relative to stationary cells (37) (PMID: 27288584). The differentiation status of stem cells can also influence cellular stiffness as exemplified in mouse embryonic stem cells (mESC) where undifferentiated mESC displays lower stiffness relative to early differentiating mESC (38) (PMID: 21728815). In addition, various pathological conditions can also influence on the stiffness of cells. Examples include arthritis, asthma, malaria, and sickle cell anemia which can have an effect on the cell stiffness (39) (PMID: 17257698). Notably, in the context of cancer, it has been shown that cancer cells are generally less stiff than normal benign cells (40–43) (PMID: 10394623, 15722433, 16701805, 18654431).

2 MATERIAL AND METHODS

2.1 Cell culture

The human colon cancer cell line HCT116 (American Type Culture Collection - CCL-247) was cultured in McCoy's 5A medium (Merc) supplemented with 10 % FBS and 1 % penicillin/streptomycin (Thermo Fisher Scientific) at 37 °C in a humidified atmosphere containing 5 % CO_2. The cells were routinely tested for the presence of mycoplasma contamination (MycoAlert Mycoplasma Detection Kit - Lonza). For ultrasounds (US) experiment cells were grown in 6 cm dishes (Nunc, cat. no: 150326) and during experiments (outside of the cell incubator), cells were kept in "CO_2 Independent Medium" (Thermo Fisher Scientific) supplemented with 10 % FBS and 1 % penicillin/streptomycin.

To facilitate segmentation during image analysis, cells were labeled with a fluorescent dye prior to US treatment. Labeling was performed by incubating the cells for 30 min in serum free McCoy's 5A medium containing either 1 μM CellTracker Green CMFDA or 10 μM CellTracker Orange CMTMR (both from Thermo Fisher Scientific). For induction of epithelial-mesenchymal transition (EMT) in the epithelial HCT 116 cell line, cells were grown in the presence of 20 ng/mL recombinant TNF-α (Merc, cat. no: H8916) for 48 hours as previously described (44). To prepare a mixed culture of differently labeled EMT induced and native cells, EMT induced (48 hrs TNF-α treatment) and native HCT116 cells were separately labeled with CellTracker Green CMFDA or CellTracker Orange CMTMR, respectively. Next, the labeled cells were trypsinized, mixed in a 1:2 ratio, plated out in 6 cm dishes with McCoy's 5A (without TNF-α) and cultured for 24 hours before US treatment.

2.2 Mechanical stimulation

2.2.1 Annular transducer

The transducer is based on a piezo ring (PZT 4, outer diameter × inner diameter × thickness = $35 \times 15 \times 5\ \text{mm}^3$ - PiezoElements) fitted with a semi-spherical acoustic lens molded on the ceramic out of epoxy resin (Araldite 2020) (see Figure 1). After soldering the electrods on the piezo ring, the lens is casted on it from a mold accommodating the ring with degassed clear epoxy resin. The mold is made of cured silicon using a replication kit (Mold-It (**?**)) from an initial 3D print (Ultimaker 2+, 100 μm vertical layer size).

To reduce acoustic impedance contrast and thus increase acoustic waves transmission, the empty space of the lens is filled with degassed type-II water and the top and bottom parts are sealed using UV glue (Express Glas - Casco) with 150 μm thick glass cover slips of diameter ?? and 50 mm respectively. A special care is given to the absence of air bubbles in the filling area to ensure consistent acoustic properties and a light path for the stroboscopic imaging (see 2.3.2) comporting only elements orthogonal to the direction of the illumination.

The transducer is suspended over the 6 cm Petri dish containing the cells to be probed (see 2.1) using a 3D printed holder adjustable in height and orientation. The bottom of the transducer is set parallel to the bottom of the dish at known distance of 150 μm by interferometry between the bottom of the transducer and a 50 mm diameter cover slip placed in an empty dish for the initial alignment. This alignment procedure is performed only once for a serie of experiments, considering that the geometrical properties of the different dishes used are identical.

2.2.2 Signal generation and amplification

The signals send to the transducer are generated by the arbitrary wave generator of a TiePie Handyscope HS5 (TiePie Engineering) and then amplified by an AE Techron 7228
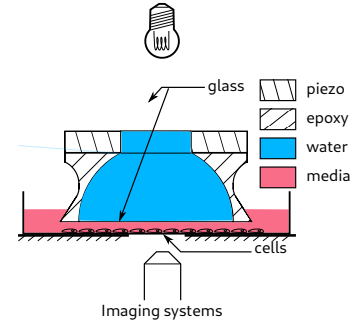

Figure 1: Overview of the setup used for mechanical stimulation of cells. WILL be edited to match the style of the other figures. ADD real image of the setup?

broadband amplifier set at maximal, calibrated, gain. The signals used are Gaussian pulses of the equation:

$$f(t) = e^{-\alpha^2 (t-t_0)^2} \sin(2\pi f_0 t) \qquad (1)$$

where f_0 is the central frequency ($f_0 = 45\ \text{kHz}$ for the experiments presented here) and t_0 the time at which the maximal amplitude of the Gaussian envelope is reached. In frequency domain, these pulses are Gaussians centered around the central frequency f_0 and of standard deviation $\sqrt{2}\alpha$ ($\alpha = 10\ \text{kHz}$ for the experiments presented here). The pre-amplified amplitude of these pulses is ranged from 5 to 20 Vpp leading to a driving voltage of 400 Vpp of the piezo[1]. The sampling frequency of the signal is set to fifty times the central frequency f_0 of the generated pulse.

The pulses are repeated N times ($N = 1000$ for the experiments presented here) at a constant frequency f_{repet} ($f_{\text{repet}} = 1\ \text{kHz}$ for the experiments presented here), allowing time for the waves to fade out between the successive pulse preventing the formation of stationary waves. Each pulse is centered in the repetition period hence: $t_0 = \frac{1}{2 f_{\text{repet}}}$.

2.2.3 Tracers

Before the experiment, the cell medium is seeded with non fluorescent tracers (Polyscience Inc. - Polybead) of a diameter $d = 3\ \mu\text{m}$. The maximum velocity attained by these beads in experiments being of the order of 1 m/s, thus the Stokes number of these particles is in the order of 10^{-2} which ensures that they are following the flow accurately.[2]

2.3 Imaging

All experiments are performed at room temperature on an inverted motorised microscope (IX81 - Olympus) controlled with μManager (45). The microscope is fitted with both a fast camera for stroboscopic imaging and a high sensitivity camera for fluorescence. These two cameras are mounted

---

[1]to be checked
[2]to be extended

on the side and the eye port respectively. Fluorescence and stroboscopic imaging are performed sequentially to ensure that the acquired fluorescence signals have not been impacted by a previous mechanical stimulation. Stroboscopic imaging is performed right after the fluorescence acquisition on the same field of view.

2.3.1 Fluorescence imaging

Fluorescence imaging is performed with a low-noise camera (Zyla sCMOS - Andor) controlled alongside the microscope with μManager (45). Illumination is provided by a broad spectrum mercury lamp (U-LH100HG - Olympus) before being fed to standard fluorescence cubes. The intensity of the light is set low enough to avoid photo-bleaching during the time of the experiment by using neutral density filters with optical densities of 0.2 or 0.6.

For the experiments presented here, fluorescence images were acquired at a rate of 2 Hz at 12 bits depth. Acquisition was started between one and two minutes before the ultrasonic exposure in order to ensure both a stabilization of the properties of the camera and to acquire control images of the system before any mechanical stimulation [3].

2.3.2 Stroboscopic imaging

Stroboscopy is a technique allowing to recover fast periodic motions by imaging them at a lower frequency, close or at an integer divider of the phenomenon frequency. When this is done with a short enough exposure time, the original motion is aliased at lower frequencies, appearing slower or even stationary, as it can be seen for example in movies where the wheels of vehicles appear to move slower or in opposite direction than they actually do. According to the Nyquist-Shannon theorem, imaging a cells' motion at ultrasonic frequencies require an imaging speed of at least two times the ultrasonic frequency. For the experiments presented here, where the ultrasonic frequency used is 45 kHz, imaging at, at least 90 fps would be needed to recover the motion occurring at the US frequency. On modern fast camera such framerates can usually be accessed by reducing the captured field of view leading to a smaller probed material. Using stroboscopy, a large field of view can be recorded using a lower framerate while still recovering the fast motion occurring at US frequency. Stroboscopic imaging is performed using a fast camera (Fastcam mini WX - Photron) under phase contrast illumination provided by the microscope built-in lamp at full power through the transducer (see 2.2.1). The frame acquisition is triggered by an external generator (Tektronix - AFG1062) which is clock-synchronised with the arbitrary waveform generator of the TiePie (see 2.2) that is used for signal generation. Frame acquisition rate f_{strobo} is set so that the equivalent of a full pulse is imaged during

---

[3]to be reformulated, a bit wobbly...

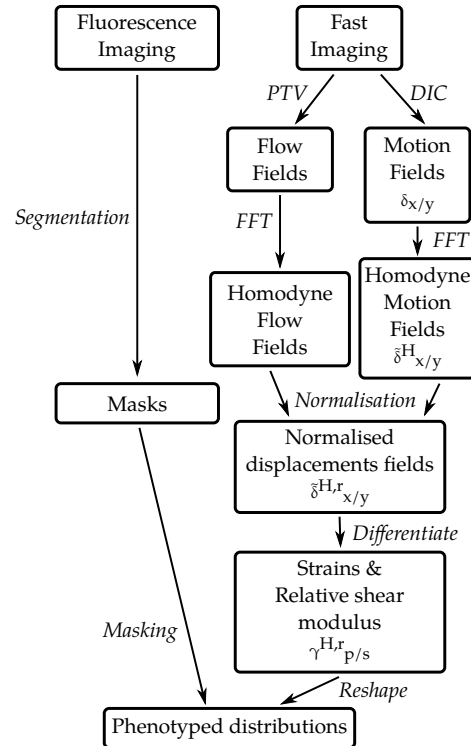
Figure 2: Workflow diagram of the analysis process.

the repetitions, hence:

$$f_{strob} = \frac{N}{N+1} f_{repet} \qquad (2)$$

where N is the total number of pulses and f_{repet} the repetition rate of the pulses (see 2.2). Following this, one image is acquired for each pulse leading to a minimal sequence of N images for complete motion recovery. In practice, a greater number (typically $N_{aq} = 3N/2$) of images are acquired in order to be used as reference images. Both the camera and the triggering generator are triggered upon start by the TiePie ensuring no jittering between the experiments.

The exposure time of the camera is set to the lowest value yielding usable images and is always under $1/200$ ms. The exposure time is set to be at least four times smaller than the period of the stimulation ($1/f_0$) ensuring good stroboscopic conditions. Post-experiment reconstruction is done by considering that adjacent frames are to be separated by a constant amount of time $\delta t = 1/f_{strob} - 1/f_{repet}$.

2.4 Data analysis

An overview of the data analysis process is shown in Fig. 2, the different steps are detailed below.

2.4.1 Flow estimation

Particle Tracking Velocimetry (PTV) is performed using FAST (46) on the tracers located in the same focal plane as the
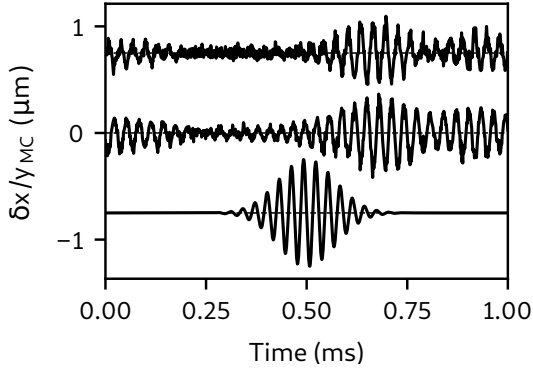
Figure 3: Typical displacements recovered alongside X (top) and Y axis (middle) versus time. The signal sent to the generator is depicted on arbitrary units at the bottom for comparison. WILL be edited to match the style of the other figures

biological cells studied. For each frame particle displacements are averaged regardless of the position in space of the beads, leading to the averaged flow velocity in the field of view of the experiment.

2.4.2 Segmentation

Segmentation is performed on the images acquired with the fluorescence imaging system (see 2.3.1). All fluorescent images are first averaged to increase the signal over noise ratio. Long range heterogeneity in the illumination is computed using a Gaussian blur with a kernel size that is half the images' size. This background is substracted to the averaged image and the result is segmented to identify biological material in the field of view by standard threshold. ADD: sensibility to the masks??

2.4.3 Homodyne cell motion estimation

Standard digital image correlation is used on every image to obtain displacements $\delta_x(t)$ and $\delta_y(t)$ in the x and y directions with respect to a reference image. A new, homodyne computation of strains from the displacements ensures a very good signal to noise ratio...

Biological material motion maps $\delta_{x/y}(x, y)$ are extracted, pixel-wise for the horizontal (x) and vertical (y) directions, by digital image correlation (DIC) against an averaged image (with no strain) obtained straight after the US. DIC is performed using the `MM2DPosSism` subprogram of MicMac (47) with a comparison box of $5 \times 5\,\text{pixel}^2$. An example of recovered displacements, and a comparison with the input signal is shown in Fig. 3. The waveforms of the recovered displacements display the same central/carrier frequency f_0 as the input signal, with an envelope encompassing both the main pulse, centered at $t_0 \approx 0.70\,\text{ms}$, and an echo which, because of the stroboscopic recording, folds back at the beginning of

the movie.

Using Fast Fourier Transform (FFT) of the displacements $\tilde{\delta}_{x/y}(f) = \underline{\delta}_{x/y} e^{i\phi_{x/y}}$, where i is the imaginary unit, are computed. An homodyne detection is then performed by only keeping the amplitude and phase at the carrier frequency f_0:

$$\tilde{\delta}^{\mathrm{H}}_{x/y} = \underline{\delta}^{\mathrm{H}}_{x/y} e^{i\phi^{\mathrm{H}}_{x/y}} = \tilde{\delta}_{x/y}(f = f_0) \qquad (3)$$

This leads to pixel-wise homodyne amplitude $\underline{\delta}^{\mathrm{H}}_{x/y}$ and phase $\phi^{\mathrm{H}}_{x/y}$ maps (see Fig. 4). Phase maps are unwrapped using the algorithm from Herráez $et\ al.$ (48) before further analysis.

For comparison between experiments, normalised homodyne displacement amplitudes $\underline{\delta}^{\mathrm{H,\,r}}_{x/y}$ are computed as the ratio between the homodyne displacement amplitudes of the biological material and the homodyne components of the flow which are similarly computed as the amplitudes of the FFT of the averaged tracer displacements (see 2.4.1) at the carrier frequency f_0, alongside both X and Y directions.

Both amplitude and phase maps are then mapped to the same shape as the fluorescence images (see 2.3.1) using an affine transformation with bi-linear interpolation. This leads to a direct pixel to pixel correspondence between the images acquired with the two imaging systems.

2.4.4 Homodyne strains computation

From bi-dimensional displacement maps $\delta_{x/y}(x, y)$, pure and simple shear strains can be classically calculated as:

$$\gamma_{\mathrm{p}} = \frac{\partial \delta_x}{\partial x} + \frac{\partial \delta_y}{\partial y} \qquad (4)$$

$$\gamma_{\mathrm{s}} = \frac{\partial \delta_x}{\partial y} + \frac{\partial \delta_y}{\partial x} \qquad (5)$$

respectively.

Analogous, homodyne strains are computed from the homodyne displacements maps $\tilde{\delta}_{x/y}$ (see 2.4.3):

$$\gamma_{\mathrm{p}}^{\mathrm{H}} = \frac{\mathrm{D}\tilde{\delta}_x}{\mathrm{D}x} + \frac{\mathrm{D}\tilde{\delta}_y}{\mathrm{D}y} \qquad (6)$$

$$\gamma_{\mathrm{s}}^{\mathrm{H}} = \frac{\mathrm{D}\tilde{\delta}_x}{\mathrm{D}y} + \frac{\mathrm{D}\tilde{\delta}_y}{\mathrm{D}x} \qquad (7)$$

with D an $homodyne\ differentiation$ scheme defined for a complex function $\tilde{f} : x \mapsto \tilde{f}(x) = \underline{f}(x)e^{i\phi(x)}$ as:

$$\frac{\mathrm{D}\tilde{f}(x)}{\mathrm{D}x} =$$

$$\lim_{\delta \to 0} \frac{1}{4\delta} \int_0^{2\pi} \left| \underline{f}(x) \cos\left(\phi(x) + s\right) \right.$$
$$\left. - \underline{f}(x + \delta) \cos\left(\phi(x + \delta) + s\right) \right| \mathrm{d}s \qquad (8)$$

ADD: physical meaning: the average of the absolute difference between two signals.

It can be shown (see SM) that this scheme can be efficiently computed as:

$$\frac{\mathrm{D}\tilde{f}(x)}{\mathrm{D}x} = \lim_{\delta \to 0} |\tilde{f}(x) - \tilde{f}(x + \delta)| \qquad (9)$$

This scheme is applied on the amplitude and phase components from DIC (see 2.4.3) of neighboring pixels. For instance:

$$\frac{\mathrm{D}\tilde{\delta}_x}{\mathrm{D}}(x_0, y_0) =$$
$$\frac{1}{4} \int_0^{2\pi} \left| \underline{\delta}(x_0) \cos(\phi_x(x_0) + s) \right.$$
$$\left. - \underline{\delta}(x_0 + 1) \cos(\phi_x(x_0 + 1) + s) \right| \mathrm{d}s \qquad (10)$$

allowing to numerically compute the homodyne strains defined in Eqs. 6 and 7 using a Simpson integration scheme.[4]

Similarly, normalised homodyne strains $\gamma_p^{\mathrm{H,r}}$, $\gamma_s^{\mathrm{H,r}}$ are computed in the same fashion using the normalised displacements $\tilde{\delta}_{x/y}^{\mathrm{H,r}}$. An example of normalised homodyne strains maps is shown in Fig. 5.

2.4.5 Relative shear modulus derivation

The shear modulus of a material is commonly defined as the ratio between the shear stress, σ and the shear strain γ. We consider that the shear stress to which the material is submitted here is *proportional* to the fluid velocity surrounding the material: $\sigma \propto v_{fluid} \propto \gamma_{fluid}$. We are so far skipping the fact that the stress and strains are in the zx or zy planes, and therefore we need the thickness of the cells to get things right. It follows that, under this assumption, the normalised homodyne strains $\gamma_p^{\mathrm{H,r}}$ are proportional to the inverse of the shear modulus of the material probed:

$$G_{\mathrm{p/s}} = \sigma/\gamma... \propto 1/\gamma_{\mathrm{p/s}}^{\mathrm{H,r}} = G_{\mathrm{p/s}}^{\mathrm{r}} \qquad (11)$$

The relative shear moduli $G_{\mathrm{p/s}}^{\mathrm{r}}$ (that can be derived from both the pure and simple normalised shear components) can be computed for every area of interest and allows to compare the rigidity of different materials or even the relative rigidity of different parts of a material. An example of a relative shear modulus map, recovered from both the pure and simple strains is presented in Fig. 7.

2.4.6 Statistical analysis

3 RESULTS

3.1 Motion, strain and elastography at the cellular level

As shown in Figs 4, 5, 6 and 7 the method presented here recovers bi-dimensionnal motion, strains and elastographic

---

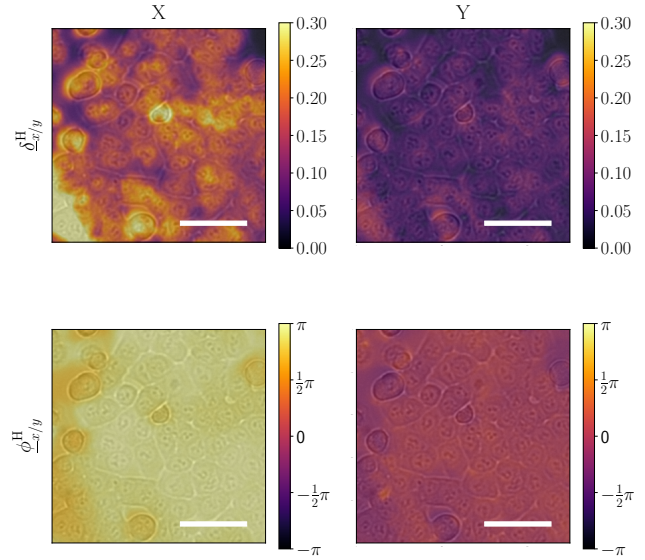[4]maybe a more detailed overview of this differentiation would be a good idea in a supplementary material?

Figure 4: Example of homodyne amplitudes $\underline{\delta}_{x/y}^{\mathrm{H}}$ (top) and phases $\phi_{x/y}^{\mathrm{H}}$ (bottom) displacements maps alongside the X (horizontal) and Y (vertical) axis respectively. Cells are of the epithelial phenotype. Scale bar is $50\,\mu\mathrm{m}$. UNITS for displacement? (Need to figure out, from the FFT)

maps of living cells on fields of view going up to the size of a colony (up to $700 \times 800\,\mu\mathrm{m}^2$ for the experiments presented here) in a single burst of US. The attainable spatial resolution of these features is principally dictated by the microscope objective used and the size of the comparison box used for the DIC and is $2.57\,\mu\mathrm{m}$ for the experiments presented here.

This resolution is smaller than the typical size of adherent cells used in *in vivo* experiments, giving access to both the imposed strains and elastographic properties at the sub-cellular level. This can be seen on Fig 6 where the local maxima of both $G_{\mathrm{p/s}}^{\mathrm{r}}$ are associated with cells' nuclei. It is worth noting, as it can be seen in Fig 4 (top) that cells' nuclei are generally associated with strong homodyne displacement components, which are homogeneous at the nuclei scale. Hence, these nuclei are showing a solid body motion with little deformation inside the cytoplasm due to their high rigidity relative to the surrounding water.

3.2 Differences of cell rigidity during EMT transition

Relative shear moduli $G_{\mathrm{p/s}}^{\mathrm{r}}$ for the two phenotypes (epithelial and mesenchymal) using the fluorescent masks (2.4.2) to differentiate the biological material from the background. $G_{\mathrm{p/s}}^{\mathrm{r}}$ are observed to be significantly different for two phenotypes (see Tab. 1 and Fig. 8) with the epithelial phenotype showing
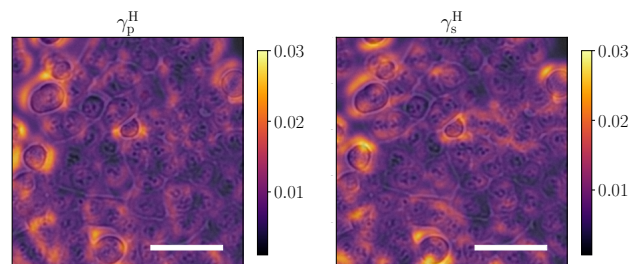
Figure 5: Prospective figure. Example of normalised homodyne shear strains, $\gamma_p^{H,r}$ (left) and $\gamma_s^{H,r}$ (right), recovered with the method presented here, superimposed with phase contrast images of the biological tissue at rest. Scale bar is $50\,\mu m$ and the view field is the same than Fig. 4.
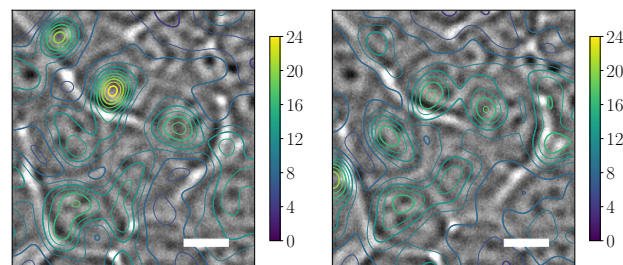

Figure 6: Close up on shear modulus maps $G_{p/s}^r$, extracted from the pure (left) and simple (right) strains maps for the epithelial phenotype. Scale bar is $10\,\mu m$

Table 1: Relative shear moduli. Confidence intervals are three standard deviation around the average value, obtained with bootstrapping. /make a box plot instead

	Epithelial	Mesenchymal
G_p^r	10.42 ± 0.05	5.15 ± 0.03
G_s^r	10.36 ± 0.05	4.87 ± 0.03

relative shear moduli two times greater than the mesenchymal phenotype. [5] For both types of cells, the relative shear moduli obtained from pure shear strain G_p^r and from simple shear strain G_s^r are very similar, showing that these two components are likely probing the same mechanical information namely the shear modulus of the biological material.

As is can be seen on Fig. 8 (grayed lines), even though the variation of the recovered moduli between experiments is significant, the two phenotypes are clearly differentiated by this technique.

3.3 Reproducibility and impact of the US on biological materials

The short duration of the experiment (1 s for the experiments presented here, see 2.3.2) allows us to probe mechanical change of the biological material on short time-scales. As the technique presented subject the biological material to a mechanical stimuli one can expect both rapid changes directly provoked by the excitation (like the breakage of adherent junctions between) and slower changes triggered by mechanotransduction mechanisms.

Repeated experiments on the same FOV have been performed for both phenotypes (see Fig. 8 inlay) with an average time between experiments of 2 and a half minutes.

Note: this has not been repeated, should I include it?

3.4 Mixed cells experiments

On-going analysis

4 CONCLUSION AND PERSPECTIVE

In this article we have a presented SOE, a new elastography technique which, by the use of a cylindrical acoustic transducer and stroboscopic fast imaging, allows to recover mechanical information on live biological material with both a high throughput as a whole FOV is probed at the same time and sub-cellular resolution. Using this technique we demonstrated the change in stiffness following EMT of human cells, and the ability to differentiate a mixed culture of the two phenotypes.

The optical resolution in this proof-of-concept, was $2.6\,\mu m$, allowing for sub-cellular components to be identified, most particularly the stiffness of the nucleus can be differentiated from that of the cytoskeleton. The resolution and the probed

---

[5] would be nice to have a citation of observed value changes in litterature
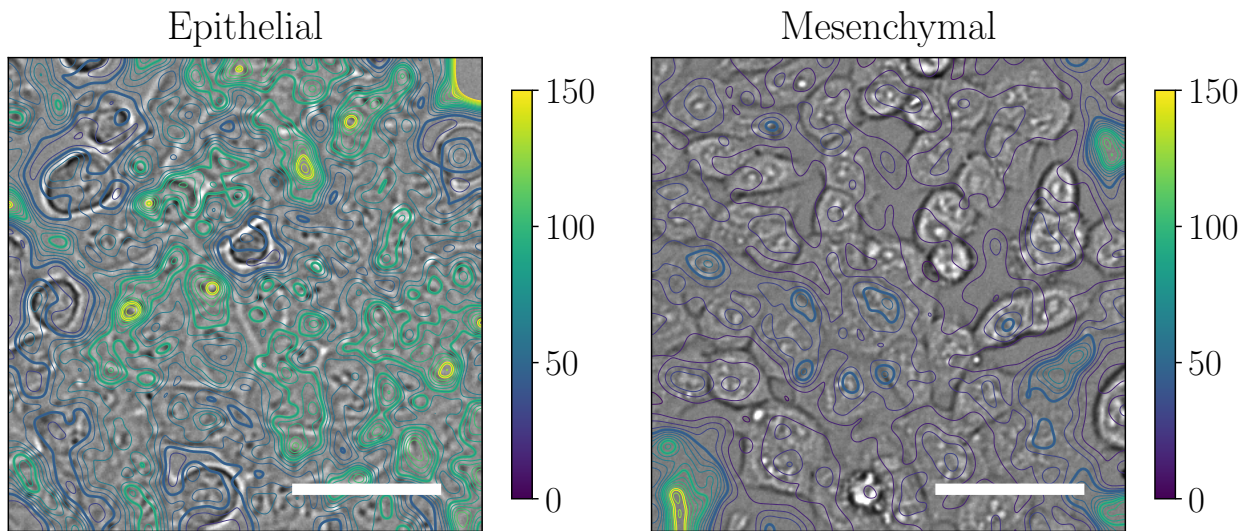
Epithelial

Mesenchymal

Figure 7: TODO: Update legend/add arrows on particular features/mention thin thirck lines what are they. Example of relative shear modulus maps $G_{p/s}^r$, extracted from the pure (left) and simple (right) strains maps. Top row: epithelial phenotype, bottom: mesenchymal phenotype. For the epithelial phenotype the field of view is the same than figures 4 and 5. Scale bar is 50 µm and the view field is the same than Figs. 4 and 5.
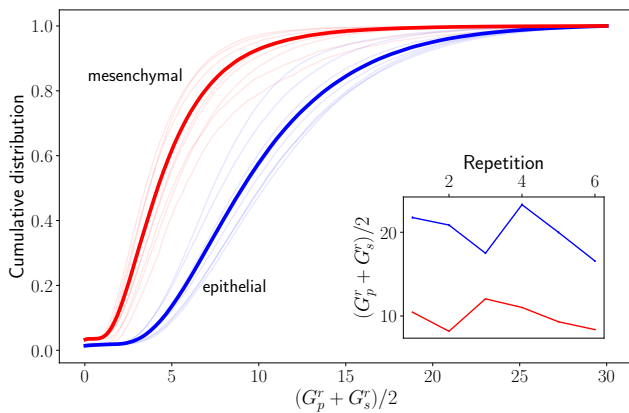

Figure 8: Cumulative distributions of relative shear moduli G_p^r (continuous line) and G_s^r (dashed line) for both epithelial (blue) and mesenchymal (red) phenotypes. Individual experiments are superimposed as grayed lines with the same color code. Inset: evolution of $G_{p/s}^r$ for same cells upon repetition of the experiment. For both experiments, the sixth repetition happened in a 13 min time frame fro the first experiment. Error bars are showing three standard deviation around the mean value, both obtained by bootstrapping.

area are only limited by the imaging system, hence, higher resolution and FOV are attainable by the use of higher or lower magnification lenses given that enough light is provided to attain the short exposure times required by the stroboscopic measurements. In that respect, the use of cylindrical hollow acoustic lenses allow good conditions for transmission illumination to allow imaging the area being insonicated. Finally, this technique is evolving in the low-ultrasonic range and provides stiffness measurements at frequencies not attainable by AFM or standard US imaging. The lower boundary of this range is limited by the possibility to build practical hollow transducer for audible frequencies, and the higher one is limited by the image acquisition (exposure time and illumination).

Bottleneck: DIC. Should I say a word on fast way to perform (establishing only a few terms of the FFT). Write on ease of implement on normal biological setup (petri dishes)

- Emphasize sensitivity (need to compute it. . .)

- emphasize compatibility with standard cell culture

- SNR ???

- Emphasize resolution (adjustable)

- throughput (adjustable)

- Comparison to other methods

4.1 Perspectives

- what can it be used for

- Use for studying mechanotransduction (very well known strains)

- Get absolute values for the moduli: height is needed or external reference

5 ACKNOWLEDGEMENTS

REFERENCES

1. Ferraioli, G., P. Parekh, A. B. Levitov, and C. Filice, 2014. Shear wave elastography for evaluation of liver fibrosis. *Journal of Ultrasound in Medicine* 33:197–203.

2. Ferraioli, G., C. Tinelli, B. Dal Bello, M. Zicchetti, G. Filice, C. Filice, and L. F. S. Group, 2012. Accuracy of real-time shear wave elastography for assessing liver fibrosis in chronic hepatitis C: a pilot study. *Hepatology* 56:2125–2133.

3. Evans, A., P. Whelehan, K. Thomson, D. McLean, K. Brauer, C. Purdie, L. Jordan, L. Baker, and A. Thompson, 2010. Quantitative shear wave ultrasound elastography: initial experience in solid breast masses. *Breast cancer research* 12:1–11.

4. Barr, R. G., and Z. Zhang, 2015. Shear-wave elastography of the breast: value of a quality measure and comparison with strain elastography. *Radiology* 275:45–53.

5. Woo, S., S. Y. Kim, J. Y. Cho, and S. H. Kim, 2014. Shear wave elastography for detection of prostate cancer: a preliminary study. *Korean journal of radiology* 15:346–355.

6. Sebag, F., J. Vaillant-Lombard, J. Berbis, V. Griset, J. Henry, P. a. Petit, and C. Oliver, 2010. Shear wave elastography: a new ultrasound imaging mode for the differential diagnosis of benign and malignant thyroid nodules. *The Journal of Clinical Endocrinology & Metabolism* 95:5281–5288.

7. Azeloglu, E. U., J. Bhattacharya, and K. D. Costa, 2008. Atomic force microscope elastography reveals phenotypic differences in alveolar cell stiffness. *Journal of applied physiology* 105:652–661.

8. Azeloglu, E. U., and K. D. Costa, 2009. Dynamic AFM elastography reveals phase dependent mechanical heterogeneity of beating cardiac myocytes. *In* 2009 Annual International Conference of the IEEE Engineering in Medicine and Biology Society. IEEE, 7180–7183.

9. Costa, K. D., 2004. Single-cell elastography: probing for disease with the atomic force microscope. *Disease markers* 19:139–154.

10. Maneshi, M. M., P. A. Gottlieb, and S. Z. Hua, 2017. A Microfluidic Approach for Studying Piezo Channels. *Current Topics in Membranes* 79:309–334.

11. Nyberg, K. D., S. L. Bruce, A. V. Nguyen, C. K. Chan, N. K. Gill, T.-H. Kim, E. K. Sloan, and A. C. Rowat, 2018. Predicting cancer cell invasion by single-cell physical phenotyping. *Integrative Biology* 10:218–231.

12. Style, R. W., R. Boltyanskiy, G. K. German, C. Hyland, C. W. MacMinn, A. F. Mertz, L. A. Wilen, Y. Xu, and E. R. Dufresne, 2014. Traction force microscopy in physics and biology. *Soft matter* 10:4047–4055.

13. Kennedy, B. F., P. Wijesinghe, and D. D. Sampson, 2017. The emergence of optical elastography in biomedicine. *Nature Photonics* 11:215–221.

14. Yu, W., Q.-Y. Lu, S. Sharma, C. Ly, D. Di Carlo, A. C. Rowat, M. LeClaire, D. Kim, C. Chow, J. K. Gimzewski, et al., 2020. Single cell mechanotype and associated molecular changes in urothelial cell transformation and progression. *Frontiers in Cell and Developmental Biology* 8:601376.

15. Gill, N. K., C. Ly, K. D. Nyberg, L. Lee, D. Qi, B. Tofig, M. Reis-Sobreiro, O. Dorigo, J. Rao, R. Wiedemeyer, et al., 2019. A scalable filtration method for high throughput screening based on cell deformability. *Lab on a Chip* 19:343–357.

16. Varol, R., S. Omeroglu, Z. Karavelioglu, G. Aydemir, A. Karadag, H. E. Meco, G. C. Kocal, M. E. Oruc, G. B. Esmer, Y. Basbinar, et al., 2021. Holographic Cell Stiffness Mapping Using Acoustic Stimulation. *arXiv preprint arXiv:2102.07480* .

17. Chao, P.-Y., W.-W. Liu, S.-F. You, and P.-C. Li, 2018. Shear wave elasticity measurements of three-dimensional cancer cell cultures using laser speckle contrast imaging. *Scientific Reports* 8:1–10.

18. Tseng, Y., T. P. Kole, and D. Wirtz, 2002. Micromechanical mapping of live cells by multiple-particle-tracking microrheology. *Biophysical journal* 83:3162–3176.

19. Taljanovic, M. S., L. H. Gimber, G. W. Becker, L. D. Latt, A. S. Klauser, D. M. Melville, L. Gao, and R. S. Witte, 2017. Shear-wave elastography: basic physics and musculoskeletal applications. *Radiographics* 37:855–870.

20. Kennedy, B. F., R. A. McLaughlin, K. M. Kennedy, L. Chin, P. Wijesinghe, A. Curatolo, A. Tien, M. Ronald, B. Latham, C. M. Saunders, et al., 2015. Investigation of Optical Coherence Microelastography as a Method to Visualize Cancers in Human Breast TissueImaging Human Breast Cancer Using OCME. *Cancer Research* 75:3236–3245.

21. Allen, W. M., L. Chin, P. Wijesinghe, R. W. Kirk, B. Latham, D. D. Sampson, C. M. Saunders, and B. F. Kennedy, 2016. Wide-field optical coherence microelastography for intraoperative assessment of human breast cancer margins. *Biomedical optics express* 7:4139–4153.

22. Scarcelli, G., and S. H. Yun, 2008. Confocal Brillouin microscopy for three-dimensional mechanical imaging. *Nature photonics* 2:39–43.

23. Schmitt, J. M., 1998. OCT elastography: imaging microscopic deformation and strain of tissue. *Optics express* 3:199–211.

24. Scarcelli, G., W. J. Polacheck, H. T. Nia, K. Patel, A. J. Grodzinsky, R. D. Kamm, and S. H. Yun, 2015. Noncontact three-dimensional mapping of intracellular hydromechanical properties by Brillouin microscopy. *Nature methods* 12:1132–1134.

25. Cross, S. E., Y.-S. Jin, J. Rao, and J. K. Gimzewski, 2020. Nanomechanical analysis of cells from cancer patients. *In* Nano-Enabled Medical Applications, Jenny Stanford Publishing, 547–566.

26. Nyberg, K. D., M. B. Scott, S. L. Bruce, A. B. Gopinath, D. Bikos, T. G. Mason, J. W. Kim, H. S. Choi, and A. C. Rowat, 2016. The physical origins of transit time measurements for rapid, single cell mechanotyping. *Lab on a Chip* 16:3330–3339.

27. Brillouin, L., 1922. Diffusion de la lumière et des rayons X par un corps transparent homogène. *In* Annales de physique. volume 9, 88–122.

28. Antonacci, G., V. de Turris, A. Rosa, and G. Ruocco, 2018. Background-deflection Brillouin microscopy reveals altered biomechanics of intracellular stress granules by ALS protein FUS. *Communications biology* 1:1–8.

29. Bevilacqua, C., H. Sánchez-Iranzo, D. Richter, A. Diz-Muñoz, and R. Prevedel, 2019. Imaging mechanical properties of sub-micron ECM in live zebrafish using Brillouin microscopy. *Biomedical Optics Express* 10:1420–1431.

30. Rigato, A., A. Miyagi, S. Scheuring, and F. Rico, 2017. High-frequency microrheology reveals cytoskeleton dynamics in living cells. *Nature physics* 13:771–775.

31. Tseng, Y., J. S. Lee, T. P. Kole, I. Jiang, D. Wirtz, and D. Wirtz, 2004. Micro-organization and visco-elasticity of the interphase nucleus revealed by particle nanotracking. *J Cell Sci* 117:2159–2167.

32. Stephens, A. D., E. J. Banigan, and J. F. Marko, 2018. Separate roles for chromatin and lamins in nuclear mechanics. *Nucleus* 9:119–124.

33. Guilak, F., J. R. Tedrow, and R. Burgkart, 2000. Viscoelastic properties of the cell nucleus. *Biochem Biophys Res Commun* 269:781–786.

34. Pegoraro, A. F., P. Janmey, and D. A. Weitz, 2017. Mechanical Properties of the Cytoskeleton and Cells. *Cold Spring Harb Perspect Biol* 9.

35. Zuidema, A., W. Wang, and A. Sonnenberg, 2020. Crosstalk between Cell Adhesion Complexes in Regulation of Mechanotransduction. *Bioessays* 42:e2000119.

36. Kelly, G. M., J. I. Kilpatrick, M. H. van Es, P. P. Weafer, P. J. Prendergast, and S. P. Jarvis, 2011. Bone cell elasticity and morphology changes during the cell cycle. *J Biomech* 44:1484–1490.

37. Luo, Q., D. Kuang, B. Zhang, and G. Song, 2016. Cell stiffness determined by atomic force microscopy and its correlation with cell motility. *Biochim Biophys Acta* 1860:1953–1960.

38. Pillarisetti, A., J. P. Desai, H. Ladjal, A. Schiffmacher, A. Ferreira, and C. L. Keefer, 2011. Mechanical phenotyping of mouse embryonic stem cells: increase in stiffness with differentiation. *Cell Reprogram* 13:371–380.

39. Lee, G. Y., and C. T. Lim, 2007. Biomechanics approaches to studying human diseases. *Trends Biotechnol* 25:111–118.

40. Lekka, M., P. Laidler, D. Gil, J. Lekki, Z. Stachura, and A. Z. Hrynkiewicz, 1999. Elasticity of normal and cancerous human bladder cells studied by scanning force microscopy. *Eur Biophys J* 28:312–316.

41. Guck, J., S. Schinkinger, B. Lincoln, F. Wottawah, S. Ebert, M. Romeyke, D. Lenz, H. M. Erickson, R. Ananthakrishnan, D. Mitchell, J. Käs, S. Ulvick, and C. Bilby, 2005. Optical deformability as an inherent cell marker for testing malignant transformation and metastatic competence. *Biophys J* 88:3689–3698.

42. Wottawah, F., S. Schinkinger, B. Lincoln, S. Ebert, K. Müller, F. Sauer, K. Travis, and J. Guck, 2005. Characterizing single suspended cells by optorheology. *Acta Biomater* 1:263–271.

43. Cross, S. E., Y. S. Jin, J. Rao, and J. K. Gimzewski, 2007. Nanomechanical analysis of cells from cancer patients. *Nat Nanotechnol* 2:780–783.

44. Ieda, T., H. Tazawa, H. Okabayashi, S. Yano, K. Shigeyasu, S. Kuroda, T. Ohara, K. Noma, H. Kishimoto, M. Nishizaki, et al., 2019. Visualization of epithelial-mesenchymal transition in an inflammatory microenvironment–colorectal cancer network. *Scientific reports* 9:1–11.

45. Edelstein, A., N. Amodaj, K. Hoover, R. Vale, and N. Stuurman, 2010. Computer Control of Microscopes Using μManager. *Current Protocols in Molecular Biology* 92:14.20.1–14.20.17. https://currentprotocols.onlinelibrary.wiley.com/doi/abs/10.1002/0471142727.mb1420s92.

46. Combriat, T. Fast: Fast and Simple Tracker. https://github.com/tomcombriat/FAST.

47. Rupnik, E., M. Daakir, and M. P. Deseilligny, 2017. MicMac–a free, open-source solution for photogrammetry. *Open Geospatial Data, Software and Standards* 2:1–9.

48. Herráez, M. A., D. R. Burton, M. J. Lalor, and M. A. Gdeisat, 2002. Fast two-dimensional phase-unwrapping algorithm based on sorting by reliability following a noncontinuous path. *Applied optics* 41:7437–7444.